Instabilities of two-layer shallow-water flows with vertical shear in the rotating annulus

J. GULA, V. ZEITLIN† AND R. PLOUGONVEN

Laboratoire de Météorologie Dynamique, ENS and University P. and M. Curie, 24,
rue Lhomond 75005, Paris, France

Being motivated by the recent experiments on instabilities of the two-layer flows in the rotating annulus with super-rotating top, we perform a full stability analysis for such system in the shallow-water approximation. We use the collocation method which is benchmarked by comparison with analytically solvable one-layer shallow-water equations linearized about a state of cyclogeostrophic equilibrium. We describe different kinds of instabilities of the cyclogeostrophically balanced state of solid-body rotation of each layer (baroclinic, Rossby–Kelvin (RK) and Kelvin–Helmholtz (KH) instabilities), and give the corresponding growth rates and the structure of the unstable modes. We obtain the full stability diagram in the space of parameters of the problem and demonstrate the existence of crossover regions where baroclinic and RK, and RK and KH instabilities, respectively, compete having similar growth rates.

1. Introduction

For the study of frontal instabilities, there is a long tradition in geophysical fluid dynamics (GFD) to consider experiments on fronts in differentially rotating annuli (Hide 1958; Fultz *et al.* 1959; Hide & Fowlis 1965; Hart 1972). Recently the interest to such experiments was revived in the context of the so-called spontaneous emission of inertia-gravity waves by balanced flows (see Ford 1994; O'Sullivan & Dunkerton 1995 and the references in the special collection of Journal of the Atmospheric Sciences on this subject, Dunkerton, Lelong & Snyder 2008). Thus, short-wave patterns coupled to the baroclinic Rossby waves were observed in independent experiments (Lovegrove, Read & Richards 2000; Williams, Haine & Read 2005; Flor 2008) on instabilities of the two-layer rotating flows in the annulus at high enough Rossby numbers. Motivated by these experiments we undertake in what follows a thorough stability analysis of a two-layer shallow-water system in the rotating annulus. Classical baroclinic instability is of course recovered, but special attention is paid to unbalanced instabilities, and in particular to the RK one which we have also studied recently in the plane-parallel channel (Gula, Plougonven & Zeitlin 2009) in the linear and nonlinear regimes. The experiments mentioned above are not strictly speaking shallow-water ones, although no pronounced vertical structure was observed, as to our knowledge. The results we present below may serve, nevertheless, to understand the vertically averaged behaviour of the full system. Moreover, Williams *et al.* (2005) interpreted their experiments in terms of shallow-water dynamics, referring to Ford (1994). Being standard in GFD, the two-layer shallow-water approximation is a reasonable compromise between the realistic representation of the observed fluid flow and the computational effort (and

† Email address for correspondence: zeitlin@lmd.ens.fr

amount of resources) necessary for a full stability analysis. It is, in addition, self-consistent and universal. On the contrary, the fine vertical structure of the flow may vary from one experiment to another, as will be explained below.

The paper is organized as follows. We first benchmark the numerical method in §2 by comparing the analytic analysis for the one-layer shallow-water model in the rotating annulus with the numerical one (it should be emphasized that the linearized system is completely solvable 'by hand' in this case for the parabolic profile of the free surface). This section also serves to identify the normal modes of the system. Then in §3 we present the results of numerical stability analysis for the two-layer shallow water in the annulus. The instabilities in the two-layer case, as usual, result from the resonances between the lower layer and the upper layer normal modes (e.g. Cairns 1979; Sakai 1989). We quantify different kinds of instabilities and demonstrate the existence of crossover regions where the RK and baroclinic instabilities, and Kelvin–Helmholtz (KH) and RK instabilities, respectively, coexist having close growth rates.

2. One-layer shallow water in the rotating annulus

We consider the one-layer rotating shallow-water model on the f-plane in polar coordinates and study the flow in the cylindrical channel with boundaries situated at r_1 and $r_2 > r_1$. The system of equations is then written, in the rotating frame with the rotation rate $f = 2\Omega$:

$$\left.\begin{aligned}
Du - \left(f + \frac{v}{r}\right)v - r\Omega^2 &= -g\partial_r h, \\
Dv + \left(f + \frac{v}{r}\right)u &= -g\frac{\partial_\theta h}{r}, \\
Dh + h\nabla \cdot \boldsymbol{v} &= 0.
\end{aligned}\right\} \tag{2.1}$$

Here h is the depth of the layer, $\boldsymbol{v} = (u, v)$ are the radial and azimuthal velocity components, $D = \partial_t + u\partial_r + \frac{v}{r}\partial_\theta$ is the Lagrangian derivative, f is the constant Coriolis parameter and g is the gravity acceleration. The boundary conditions are free-slip: $u = 0$ at $r = r_1, r_2$.

We linearize these equations about the steady cyclogeostrophically balanced state with the depth profile $H(r)$, and corresponding velocity profile $V(r)$:

$$fV + \frac{V^2}{r} + r\Omega^2 = g\partial_r H. \tag{2.2}$$

As usual, the centrifugal acceleration $r\Omega^2$ may be hidden by redefinition of H. The linearized equations, with the same notation for the perturbations as for the full fields in (2.1), are

$$\left.\begin{aligned}
\partial_t u + \frac{V}{r}\partial_\theta u - fv - 2\frac{Vv}{r} &= -g\partial_r h, \\
\partial_t v + u\partial_r V + \frac{V}{r}\partial_\theta v + fu + \frac{Vu}{r} &= -g\frac{\partial_\theta h}{r}, \\
\partial_t h + \frac{1}{r}(rHu)_r + \frac{1}{r}H\partial_\theta v + \frac{V}{r}\partial_\theta h &= 0.
\end{aligned}\right\} \tag{2.3}$$

By introducing the time scale $f^{-1} = (2\Omega)^{-1}$, the horizontal scale $r_0 = r_2 - r_1$, the vertical scale $H_0 = H(r_1)$ and the velocity scale $V_0 = r_0\Omega$, we use non-dimensional variables from now on without changing notation. We thus obtain the following

non-dimensional equations:

$$
\left.
\begin{array}{l}
\partial_t u + \dfrac{V}{r}\partial_\theta u - v - 2\dfrac{Vv}{r} = -Bu\,\partial_r h, \\[2mm]
\partial_t v + u\partial_r V + \dfrac{V}{r}\partial_\theta v + u + \dfrac{Vu}{r} = -Bu\,\dfrac{\partial_\theta h}{r}, \\[2mm]
\partial_t h + \dfrac{1}{r}(rHu)_r + \dfrac{1}{r}H\partial_\theta v + \dfrac{V}{r}\partial_\theta h = 0,
\end{array}
\right\}
\tag{2.4}
$$

where $Bu = (R_d/r_0)^2$ is the Burger number and $R_d = (gH_0)^{1/2}/(2\Omega)$ is the Rossby deformation radius.

The normal modes are introduced in the standard way:

$$
(u(r,\theta),\, v(r,\theta),\, h(r,\theta)) = (\tilde{u}(r),\, \tilde{v}(r),\, \tilde{h}(r))\exp\left[ik(\theta - ct)\right] + c.c.,
\tag{2.5}
$$

where k is the azimuthal wavenumber ($k \in \mathbb{N}$) and c is the azimuthal phase velocity. Omitting tildes we thus get the following problem for eigenvalues c and eigenfunctions u, v, h:

$$
\left.
\begin{array}{l}
k\left(\dfrac{V}{r} - c\right)u - \left(1 + 2\dfrac{V}{r}\right)v = -Bu\,h_r, \\[2mm]
-\left(1 + \dfrac{V}{r} + V_r\right)u + k\left(\dfrac{V}{r} - c\right)v = -kBu\,\dfrac{h}{r}, \\[2mm]
-\dfrac{(rHu)_r}{r} + k\dfrac{H}{r}v + k\left(\dfrac{V}{r} - c\right)h = 0,
\end{array}
\right\}
\tag{2.6}
$$

where here and below we denote the r-derivative by the corresponding subscript, if it does not lead to confusion. It is known that for parabolic profile of H the eigenvalue problem (2.6) may be solved analytically (see Killworth 1983, where this problem was considered for the parabolic lens). Indeed by eliminating u and v

$$
\left.
\begin{array}{l}
u = \dfrac{Bu\,h_r k\left(\frac{V}{r} - c\right) + \frac{Bu}{r}kh\left(1 + 2\frac{V}{r}\right)}{\left(1 + 2\frac{V}{r}\right)\left(1 + \frac{V}{r} + V_r\right) - k^2\left(\frac{V}{r} - c\right)^2}, \\[4mm]
v = \dfrac{k\left(\frac{V}{r} - c\right)\frac{Bu}{r}kh + \left(1 + \frac{V}{r} + V_r\right)Bu\,h_r}{\left(1 + 2\frac{V}{r}\right)\left(1 + \frac{V}{r} + V_r\right) - k^2\left(\frac{V}{r} - c\right)^2},
\end{array}
\right\}
\tag{2.7}
$$

where we suppose that $(1 + 2(V/r))(1 + (V/r) + V_r) - k^2((V/r) - c)^2 \neq 0$, we obtain the following ordinary differential equation for h:

$$
\left(rH\left(\dfrac{V}{r} - c\right)h_r\right)_r - \left(V_r - \dfrac{V}{r}\right)Hh_r + F(r)h = 0,
\tag{2.8}
$$

with

$$
\begin{aligned}
F(r) = &\left[H\left(1 + 2\dfrac{V}{r}\right)\right]_r - k^2\dfrac{H}{r}\left(\dfrac{V}{r} - c\right) - \dfrac{r}{Bu}\left(\dfrac{V}{r} - c\right) \\[2mm]
&\times\left(\left(1 + 2\dfrac{V}{r}\right)\left(1 + \dfrac{V}{r} + V_r\right)\right) - k^2\left(\dfrac{V}{r} - c\right)^2.
\end{aligned}
\tag{2.9}
$$

Assuming a solid-body rotation of the fluid,

$$
V(r) = \alpha r, \quad H(r) = \beta r^2, \quad \beta = \dfrac{(1 + \alpha)^2}{8Bu},
\tag{2.10}
$$

consistently with the cyclogeostrophic balance (2.2), we get

$$(r^3 h_r)_r + \left[2\frac{1+2\alpha}{\alpha-c} - k^2 - \frac{((1+2\alpha)^2) - k^2(\alpha-c)^2)}{2\beta Bu}\right] rh = 0. \qquad (2.11)$$

$V(r)$ is the velocity relative to the rotating frame, the basic solid-body rotation of the fluid should then be given by $\alpha = 0$, but we keep the parameter α for generality.

By defining for compactness

$$A = \left[2\frac{1+2\alpha}{\alpha-c} - k^2 - \frac{((1+2\alpha)^2) - k^2(\alpha-c)^2)}{2\beta Bu}\right], \qquad (2.12)$$

we easily get the general solution of (2.11):

$$\left.\begin{aligned}
h(r) &= C_1 r^{\alpha_+} + C_2 r^{\alpha_-}, \\
\alpha_\pm &= -1 \pm \sqrt{1-A}.
\end{aligned}\right\} \qquad (2.13)$$

Solutions of the eigenproblem (2.6) must satisfy the boundary conditions $u(r_1) = u(r_2) = 0$ which gives, using (2.7),

$$\left.(\alpha-c)h_r + \frac{(1+2\alpha)h(r)}{r}\right|_{r=r_1,r_2} = 0. \qquad (2.14)$$

With the help of (2.13), we get the following algebraic system for $C_{1,2}$:

$$\left.\begin{aligned}
[\alpha_+(\alpha-c) + (1+2\alpha)]C_1 r_1^{\alpha_+-1} + [\alpha_-(\alpha-c) + (1+2\alpha)]C_2 r_1^{\alpha_--1} &= 0, \\
[\alpha_+(\alpha-c) + (1+2\alpha)]C_1 r_2^{\alpha_+-1} + [\alpha_-(\alpha-c) + (1+2\alpha)]C_2 r_2^{\alpha_--1} &= 0,
\end{aligned}\right\} \qquad (2.15)$$

and the solvability condition

$$[\alpha_+(\alpha-c) + (1+2\alpha)][\alpha_-(\alpha-c) + (1+2\alpha)]\left[r_1^{\alpha_+-1}r_2^{\alpha_--1} - r_1^{\alpha_--1}r_2^{\alpha_+-1}\right] = 0. \qquad (2.16)$$

Two different solutions for A, cf. (2.13), thus arise:

$$A = 2\frac{1+2\alpha}{\alpha-c} - \left(\frac{1+2\alpha}{\alpha-c}\right)^2, \qquad (2.17)$$

or

$$A = 1 + \left(\frac{n\pi}{\log(\frac{r_1}{r_2})}\right)^2, \quad n = 0, 1, 2, \ldots. \qquad (2.18)$$

2.1. Kelvin modes

The first solution (2.17) combined with (2.12) gives a fourth-order equation for the phase speed c:

$$(\alpha-c)^4 - \left(\beta Bu + \left(\frac{1+2\alpha}{k}\right)^2\right)(\alpha-c)^2 + \beta Bu\left(\frac{1+2\alpha}{k}\right)^2 = 0, \qquad (2.19)$$

with the roots

$$c = \alpha \pm \sqrt{\beta Bu}, \qquad (2.20)$$
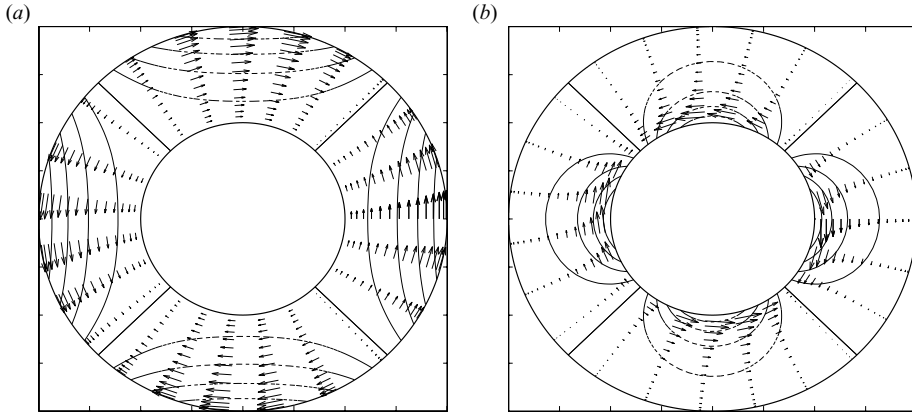
$$c = \alpha \pm \frac{1+2\alpha}{k}. \qquad (2.21)$$

FIGURE 1. Pressure and velocity fields for Kelvin modes propagating along the outer (*a*) and the inner (*b*) wall with wavenumber $k = 2$. These modes correspond to (*b*) and (*d*), respectively, in figure 3.

The first pair of roots (2.20) are non-dispersive and correspond to the eigenfunction $u \equiv 0$. They, thus, describe the two Kelvin modes concentrated at the inner and outer walls respectively. We present the elevation profile

$$h(r) = C_1 r^3 \text{ or } h(r) = C_2 r^{-3}, \tag{2.22}$$

and the corresponding velocity field obtained from (2.7) and (2.10) for Kelvin modes, with $k = 2$, in figure 1. The structure of the Kelvin waves with the wind parallel to the boundaries and pressure extrema near the lateral boundaries is clearly seen, as well as the geostrophic character of the waves. The second pair of roots (2.21) correspond to the degenerate case $(1 + 2(V/r))(1 + (V/r) + V_r) - k^2((V/r) - c)^2 = 0$ (see the previous section). As is easy to see from (2.6), or directly from (2.14) they do not correspond to any non-trivial eigenfunction and will be discarded in what follows.

2.2. *Rossby and Poincaré modes*

The second solution (2.18) combined with (2.12) gives a third-order equation for the phase speed c for each value of $n \in \mathbb{N}$:

$$\frac{k^2}{\beta Bu}(\alpha - c)^3 - \left[k^2 + 1 + \left(\frac{n\pi}{\log(\frac{r_1}{r_2})}\right) + \frac{1 + 2\alpha}{\beta Bu}\right](\alpha - c) + 2(1 + 2\alpha) = 0. \tag{2.23}$$

For each $n \in \mathbb{N}$ a set of solutions consists of one Rossby mode and two Poincaré (inertia-gravity) modes of order n.

The solutions are given, cf (2.13), by

$$h(r) = C_1 r^{[in\pi/\log(r_1/r_2)-1]} + C_2 r^{-[in\pi/\log(r_1/r_2)-1]} \tag{2.24}$$

with the constraint

$$\frac{C_1}{C_2} = -\frac{(\alpha - c)\alpha_- + (1 + 2\alpha)}{(\alpha - c)\alpha_- + (1 + 2\alpha)} \frac{r_1^{\alpha_-}}{r_1^{\alpha_+}}. \tag{2.25}$$

It should be noted that the case $n = 0 \Rightarrow A = 1$ is degenerate: the corresponding field may be obtained, as usual, by taking the limit and leads to the logarithmic in r solution.

The structure of the corresponding modes for $k = 2$ is represented in figure 2: the Rossby wave in figure 2(*a*) and the gravity wave in figure 2(*b*). The characteristic
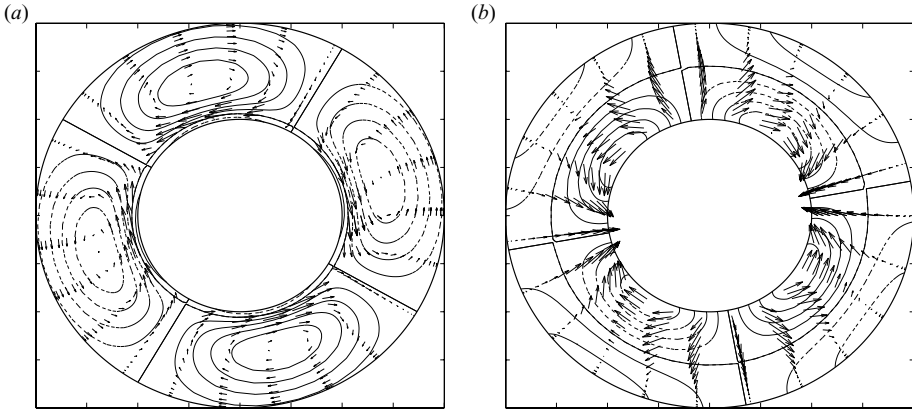
FIGURE 2. Pressure and velocity fields for $n = 1$ mode of the Rossby wave (a) and the Poincaré wave (b) for wavenumber $k = 2$. These modes correspond to (c) and (a), respectively, in figure 3.
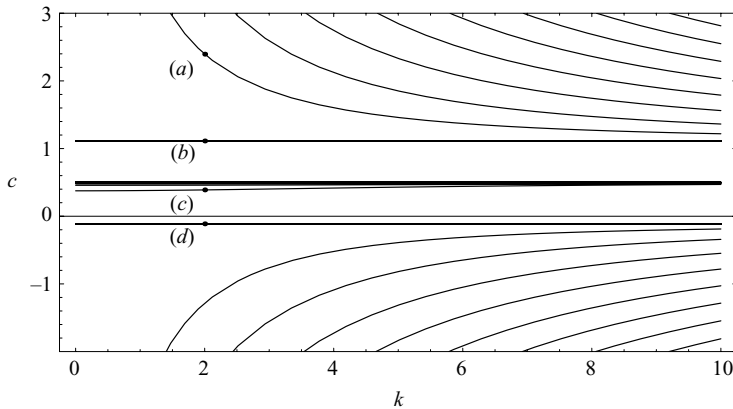

FIGURE 3. Dispersion diagram $c = c(k)$ for the solutions of (2.23) and (2.19) with $\alpha = 1/2$. (a) Poincaré modes (see figure 2b), (b) and (d) Kelvin modes (see figure 1), (c) Rossby modes (see a zoom of this part in figure 4). Note the spectral gap, i.e. the fact that fast Poincaré and Kelvin modes are separated from slow Rossby modes. Although the spectrum of k is discrete, for the sake of visualization we present continuous curves $c(k)$; it is to be kept in mind that only the values $k \in \mathbb{N}$ correspond to realizable solutions.

velocities and pressure fields of the Rossby wave are easily recognizable with wind turning around pressure extrema according to the geostrophic balance.

In figure 3 we present the dispersion diagram for thus obtained eigensolutions of the problem (2.6). It is instructive to compare this diagram with the corresponding diagrams for one-layer shallow-water flow with linear shear (Couette flow) in the rectilinear channel in the absence of rotation, as obtained in Knessl & Keller (1995) and Balmforth (1999). In the latter case, Rossby and Kelvin modes are absent; there is no spectral gap and the dispersion curves for left-moving and right-moving Poincaré modes can intersect leading to instability, according to the standard rules (Cairns 1979; Sakai 1989). In our case such intersections are not possible due to the spectral gap introduced by rotation, and the flow is stable.

We used the above-described analytic results in order to benchmark the numerical method which we are using. The eigenvalue problem of order 3 corresponding to
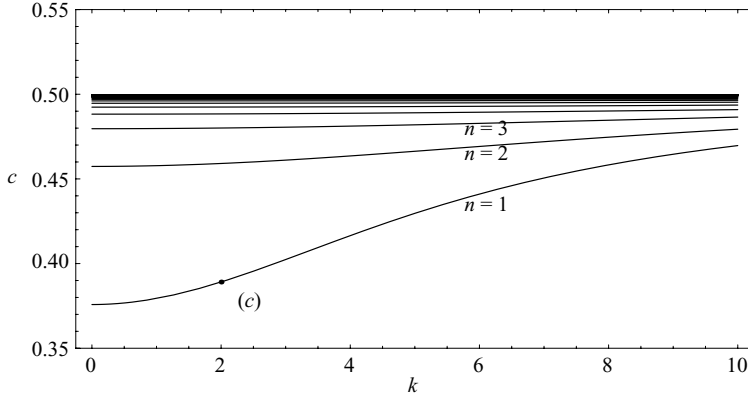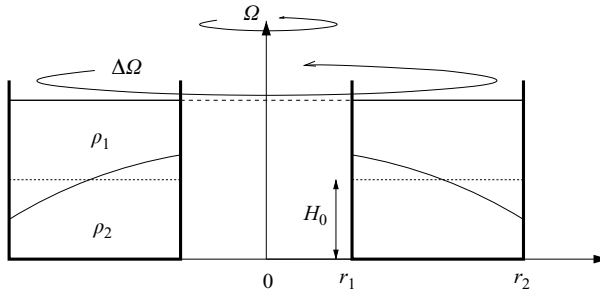
FIGURE 4. Zoom of the figure 3 on slow Rossby modes with varying n.

FIGURE 5. Schematic representation of a two-layer flow in the annulus
with a super-rotating lid.

the system of equations (2.6) can be solved numerically by applying the spectral collocation method as described in Trefethen (2000) and Poulin & Flierl (2003). A complete basis of Chebyshev polynomials is used to obtain a discrete equivalent of the system which is achieved by evaluating (2.6) on a discrete set of N collocation points (typically a rather low resolution $N = 50$ to 100 is sufficient, see below) and using the Chebyshev differentiation matrix to discretize the spatial derivatives. The eigenvalues and eigenvectors of the resulting operator are computed with the help of Matlab routine 'eig'. The occurrence of spurious eigenvalues is common in such discretization procedure. We therefore checked the persistence of the obtained eigenvalues by recomputing the spectrum with increasing N. The comparison of numerical and analytic results shows excellent agreement. We do not display it because of absence of any differences. This means that the collocation method works remarkably well even at rather low resolution.

3. Two-layer shallow water in the rotating annulus

A typical configuration used in laboratory experiments by Williams *et al.* (2005) and Flor (2008) is presented in figure 5. The annulus has an inner vertical sidewall of radius r_1, an outer vertical sidewall of radius r_2 and a total depth $2H_0$. The radial width of the annulus is therefore $r_2 - r_1$, and the two layers have equal depths H_0 at rest. The base and the lid are both horizontal and flat. The angular velocity about the axis of symmetry is Ω, and the upper lid is super-rotating at $\Omega + \Delta\Omega$. This differential

rotation provides a vertical velocity shear of the balanced basic state which is close to solid body rotation of each fluid layer, with different angular velocities. In the stability analysis which follows such state will be represented by a state of cyclogeostrophic equilibrium in each layer with linear radial profile of the azimuthal velocity in the rotating two-layer shallow-water model in the f-plane approximation.

In order to fulfil a complete linear stability analysis we use below the collocation method, benchmarked in the one-layer case. We present the model, its linearized version and introduce the key parameters in §3.1. We then display the instabilities, their growth rates and the structure of the unstable modes in §3.2.

3.1. *Overview of the model and the method*

Consider the two-layer rotating shallow-water model on the f-plane. The momentum and continuity equations are written in polar coordinates as follows:

$$\left.\begin{aligned} D_j u_j - \left(f + \frac{v_j}{r}\right) v_j - r\Omega^2 &= \partial_r \Pi_j, \\ D_j v_j + \left(f + \frac{v_j}{r}\right) u_i &= \frac{\partial_\theta \Pi_i}{r}, \\ D_j h_j + h_j \boldsymbol{\nabla} \cdot \boldsymbol{v}_j &= 0, \end{aligned}\right\} \tag{3.1}$$

where $\boldsymbol{v}_j = (u_j, v_j)$, h_j and Π_j are the (radial, azimuthal) velocity, thickness and pressure normalized by density (geopotential), in the jth layer (counted from the top) and $j = 1, 2$. Here, $f = 2\Omega$ is the dimensional background rotation and D_j denote Lagrangian derivatives in respective layers. The boundary conditions are $u = 0$ at $r = r_1, r_2$.

By introducing the time scale $1/f$, the horizontal scale $r_0 = r_2 - r_1$, the vertical scale H_0 and the velocity scale $V_0 = r_0\Omega$, we use non-dimensional variables from now on without changing notation. By linearizing about a steady state with constant azimuthal velocities $V_1 \neq V_2$, we obtain the following non-dimensional equations (the ageostrophic version of the Phillips model in cylindrical geometry):

$$\left.\begin{aligned} \partial_t u_j + \frac{V_j}{r}\partial_\theta u_j - v_j - 2\frac{V_j v_j}{r} &= -Bu\,\partial_r \pi_j, \\ \partial_t v_j + u_j \partial_r V_j + \frac{V_j}{r}\partial_\theta v_j + u_j + \frac{V_j u_j}{r} &= -Bu\frac{\partial_\theta \pi_j}{r}, \\ \partial_t h_j + \frac{1}{r}(r H_j u_j)_r + \frac{1}{r}H_j \partial_\theta v_j + \frac{V_j}{r}\partial_\theta h_j &= 0, \end{aligned}\right\} \tag{3.2}$$

where the pressure perturbations in the layers π_j are related through the interface perturbation η, as usual:

$$\pi_2 - \pi_1 + s(\pi_2 + \pi_1) = Bu\,\eta, \tag{3.3}$$

and $Bu = (R_d/r_0)^2$ is the Burger number, $Ro = \Delta\Omega/(2\Omega)$ is the Rossby number, $R_d = (g'H_0)^{1/2}/(2\Omega)$ is the Rossby deformation radius, $g' = 2\Delta\rho g/(\rho_1 + \rho_2)$ is the reduced gravity and $s = (\rho_2 - \rho_1)/(\rho_2 + \rho_1)$ is the stratification parameter.

Although the dissipative effects are totally neglected in our analysis we will also use the following non-dimensional parameter:

$$d = \frac{\sqrt{\nu\Omega}}{H\Delta\Omega} \tag{3.4}$$

for the sake of comparison with the experimental results, where for kinematic viscosity we choose the value $\nu = 1.18.10^{-6}\,\mathrm{m}^2\,\mathrm{s}^{-1}$ which corresponds to the experiments of

Williams *et al.* (2005). We will also use a parameter $F = 1/Bu$ used as the Froude number in Williams *et al.* (2005) for the same reason.

The depth profiles $H_j(r)$ and respective velocities $V_j(r)$ in (3.2) correspond to steady cyclogeostrophically balanced state in each layer:

$$2\,V_j + \frac{V_j^2}{r} + r = \partial_r \Pi_j. \tag{3.5}$$

In spite of the introduction of the parameter d, which serves uniquely for scaling purposes, our analysis is purely inviscid. In the experiment, however, the mean axisymmetric flow is controlled by friction. Indeed, there is a positive torque due to the shear across the upper Ekman layer, and there are negative torques due to the shears across the lower Ekman layer and the Stewartson layers at the outer and inner vertical sidewalls (Stewartson 1957) acting on the quasi-inviscid interiors of both the upper and lower layers. Because the Stewartson layers are very thin, it seems plausible to neglect them and to study solutions where each layer rotates as a solid body. The rotation rates of the layers lie in the interval between the rotation rate of the base (0 in the rotating frame) and that of the upper lid (Ro in the rotating frame). Therefore, in general,

$$V_2 = \alpha_2\, r, \quad V_1 = \alpha_1\, r, \tag{3.6}$$

and we get the following expressions for the heights in the state of cyclogeostrophic equilibrium for such mean flow:

$$H_j = H_j(0) + (-1)^j \left[2\alpha_2 + \alpha_2^2 - 2\alpha_1 - \alpha_1^2 + s(2\alpha_2 + \alpha_2^2 + 2\alpha_1 + \alpha_1^2 + 2) \right] \frac{r^2}{2Bu}. \tag{3.7}$$

Hart (1972) considered the top, bottom and interfacial friction layers and found that the rotations rates are $\alpha_1 = (2 + \chi)Ro/2(1 + \chi)$ and $\alpha_2 = Ro/2(1 + \chi)$ where $\chi = (\nu_2/\nu_1)^{1/2}$ is the viscosity ratio between the two layers. If the two layers have close viscosities $\chi = 1$, it leads to $(\alpha_1, \alpha_2) = (0.75\,Ro, 0.25\,Ro)$.

A calculation based on a layerwise balance of the torques in Williams, Read & Haine (2004) gives values for (α_1, α_2) about the same order but depending on the turntable angular velocity. The direct measurements of the radial velocity profiles by Flor (2008) are closer to $(\alpha_1, \alpha_2) \approx (0.9\,Ro, 0.1\,Ro)$. We will therefore keep these last values throughout the paper, but this particular choice does not mean a generality loss, as changing the relative rotation rate just means rescaling of the Rossby number.

Supposing a harmonic form of the solution in the azimuthal direction,

$$(u_j(r,\theta),\, v_j(r,\theta),\, \pi_j(r,\theta)) = (\tilde{u}_j(r),\, \tilde{v}_j(r),\, \tilde{\pi}_j(r)) \exp[ik(\theta - ct)] + c.c., \tag{3.8}$$

where k is the azimuthal wavenumber ($k \in \mathbb{N}$), and omitting tildes we get from (3.2):

$$\left.\begin{aligned}
k(V_j - rc)iu_j - (r + 2V_j)v_j + r\partial_r \pi_j &= 0, \\
-(r + V_j + r\partial_r(V_j))iu_j + k(V_j - rc)v_j + k\pi_j &= 0, \\
-\partial_r(rH_j iu) + kH_j v + k(V_j - rc)(-1)^j \eta &= 0, \\
\pi_2 - \pi_1 + s(\pi_2 + \pi_1) &= Bu\,\eta.
\end{aligned}\right\} \tag{3.9}$$

The system (3.9) is an eigenvalue problem of order 6 which can be solved by applying the spectral collocation method similarly to the one-layer flow. In comparison to the latter case, the dispersion diagrams we obtain show that the branches of dispersion relation corresponding to different modes can intersect, thus creating instabilities of various nature. Namely, we will display below the instabilities resulting
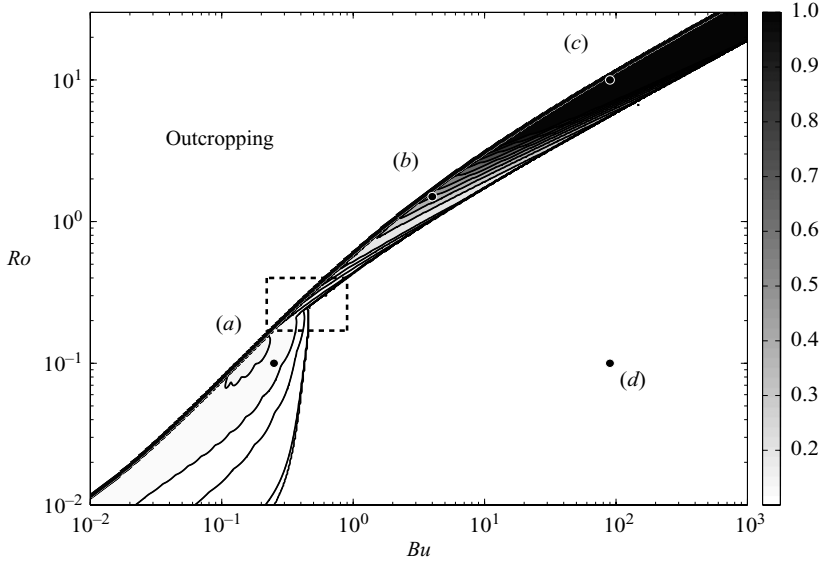
FIGURE 6. Growth rate of most unstable modes in (Ro, Bu) space. Darker zones correspond to higher growth rates. Contours displayed are 0.001, 0.01, 0.02 and further interval at 0.02. The thick upper frontier line marks the outcropping limit when the interface between the two layers intersects the bottom or the top. The results for the outcropping configuration will be not discussed in this paper.

from the interaction between Rossby waves in upper and lower layer (the baroclinic instability), the interaction between Rossby and Kelvin or Poincaré waves in respective layers (RK instability) and the interaction between two Poincaré, or Kelvin and Poincaré, or two Kelvin modes (KH instability). Although each instability occupies its proper domain in the parameter space, we will see that there exist crossover regions where two different instabilities coexist and may compete.

3.2. *Instabilities and growth rates*

We first present the overall stability diagram in the space of parameters of the model, and then illustrate different parts of this diagram by displaying the corresponding unstable modes and dispersion curves. The stability diagram was obtained by calculating the eigenmodes and the eigenvalues of the problem (3.6), (3.9) for about 50 000 points in the space of parameters (there are typically 200–300 points along each axis in the figures below) and then interpolating. As before, only discrete azimuthal wavenumbers correspond to realizable modes. We nevertheless present the results as if the spectrum of wavenumbers were continuous, for better visualization.

The results are synthesized in figures 6–9 displaying, respectively, the growth rates and the wavenumbers of most unstable modes. The results are plotted both in the plane of parameters $Ro - Bu$ (figures 6 and 7) and in the plane F and d, for convenience of comparison with laboratory experiments by Williams *et al.* (2005) (figures 8 and 9).

The parameter space is clearly divided in three different regions. The upper-left parts in all figures correspond to the outcropping (incropping) region where the interface between the layers intersects with the top (bottom) plane. The onset of out(in)cropping corresponds to the thick upper border line in the figures. The out(in)cropping situations were out of the scope of the experiments of Williams
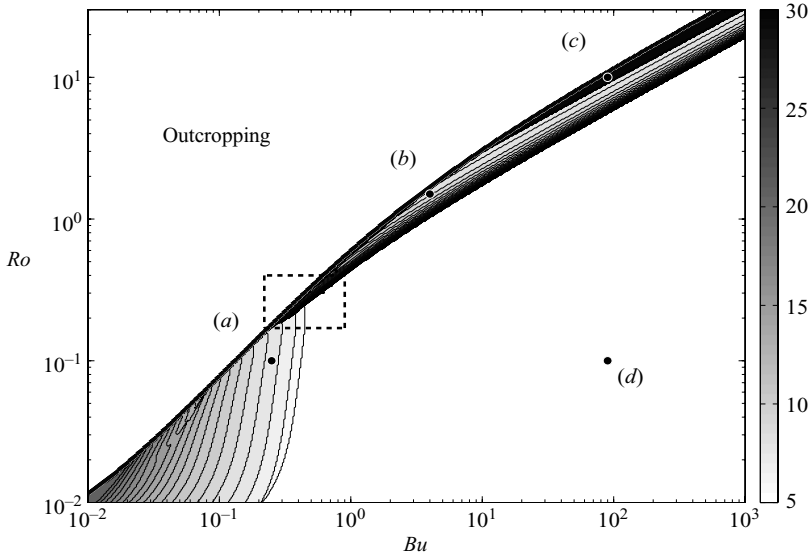
FIGURE 7. Wavenumber of most unstable modes in (Ro, Bu) space corresponding to figure 6. Darker zones correspond to higher wavenumbers. The interval between subsequent contours is 1.
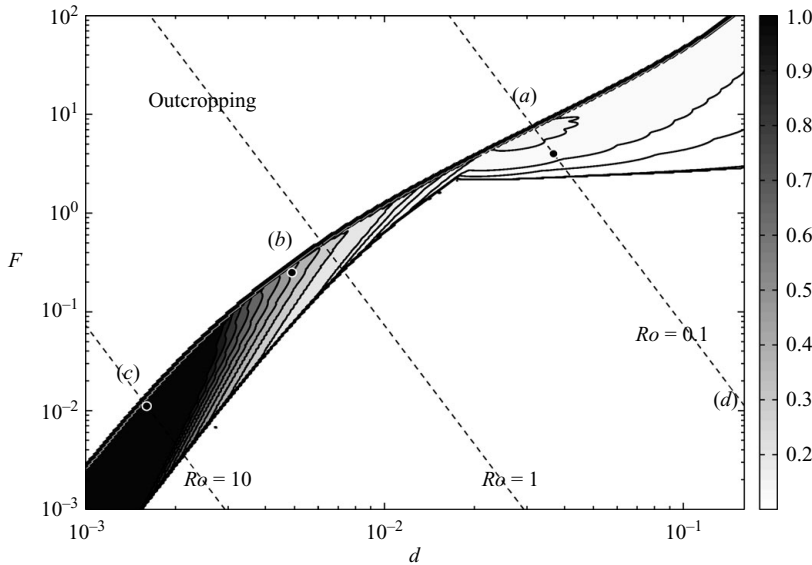

FIGURE 8. Growth rate of most unstable modes in (F, d) space. Lines of constant Ro are plotted using numerical values of Williams *et al.* (2005) for g' and H_0. Darker zones correspond to higher growth rates. Contours displayed are 0.001, 0.01, 0.02 and further at interval 0.02. The thick upper frontier line marks the outcropping limit when the interface between the two layers intersects the bottom or the top.

et al. (2005) and will be not considered in what follows. Such configurations have been studied experimentally in the classical paper by Griffiths & Linden (1982) and constitute a separate subject under current analytical and numerical investigation, which will be presented elsewhere.
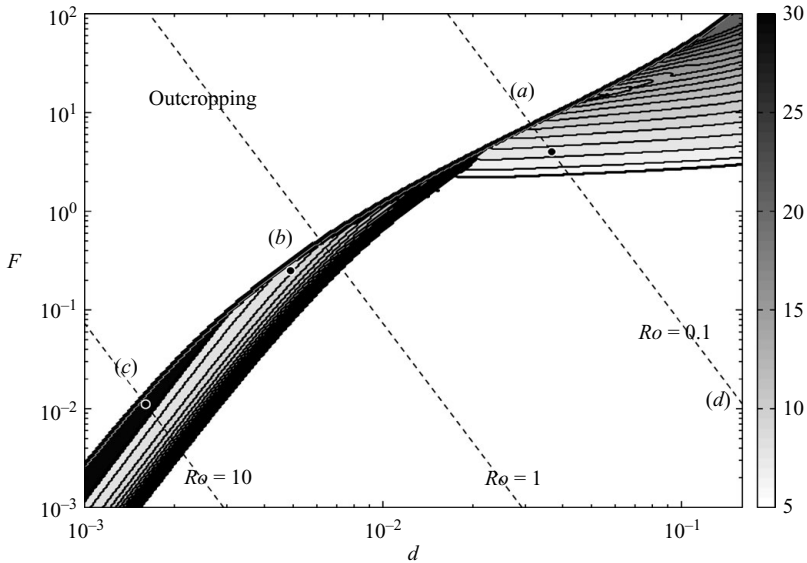
FIGURE 9. Wavenumber of most unstable modes in (F, d) space corresponding to figure 8. Darker zones correspond to higher wavenumbers. The interval between subsequent contours is 1.

The lower-right parts of all figures correspond to stable flows. An example of the dispersion diagram of such flow denoted by (d) in figure 8 is given in figure 10.

We also show in this figure how the dispersion diagrams evolve while changing parameters and approaching the instability band spreading from low-left to upper-right in figures 6–9. One clearly sees how the initially stable flow without imaginary eigenvalues of c, which is similar to the one-layer case with the same physical meaning of different branches (cf. figure 3), develops instabilities of various nature as parameters change. Thus, as shown in the left column of figure 10, decreasing the Burger number leads to distortion of the dispersion curves of Rossby modes and their reconnection leading to Rossby–Rossby (RR) resonance, i.e. the baroclinic instability. Different distortion of dispersion curves of Rossby modes takes place if Ro increases at constant Bu, leading to reconnection (a) with Kelvin-mode curve and RK resonance with corresponding instability, and (b) with Poincaré-mode curve and Rossby–Poincaré (RP) resonance and corresponding instability. Further increasing Ro leads to reconnection of Kelvin-mode curves and Kelvin–Kelvin (KK) resonance, and related KH instability. Note that although KK, KP and PP resonances are physically different, they are frequently confused in the literature and appear under the general name of KH instability. Similarly RK and RP instabilities are often called both RK (cf. Sakai 1989). We will also follow this shorthand description in what follows, which hopefully would not lead to confusion.

In the context of wave resonance, there are three essential parameters in the problem: $V = \Delta\Omega r_0$, the velocity (or velocity shear) of the basic flow, $C_R = \Omega\Delta H/H_0 r_0$, the phase velocity of the Rossby waves and $C_G = \sqrt{g'H_0}$, the phase velocity of the gravity waves. The interpretation of the results may be done on the basis of the alternative set of non-dimensional parameters which are defined as follows:

$F^* = V/C_G = \Delta\Omega r_0/\sqrt{g'H_0}$, a new Froude number and $R^* = V/C_R = g'H/2\Omega^2 r_0^2$, a new Rossby number. With these definitions one finds the baroclinic instability at
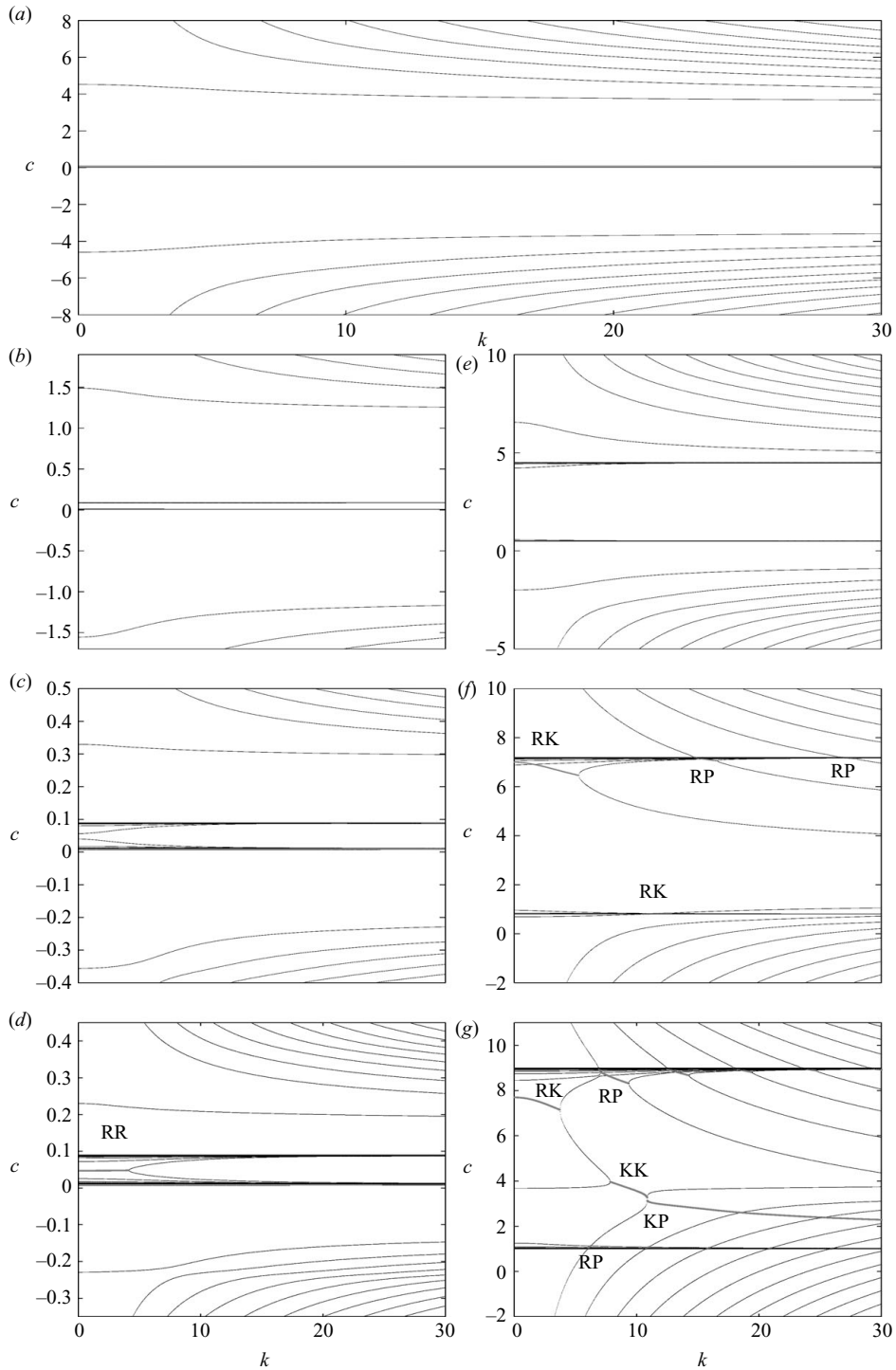
FIGURE 10. Dispersion diagram $c - k$ (*a*) for the stable configuration corresponding to point (*d*) in figure 6 and its evolution with the change of parameters: $Ro = 0.1$, Bu decreasing from top to bottom ((*a*–*d*): (*a*) $Bu = 90$, (*b*) $Bu = 10$, (*c*) $Bu = 0.5$ and (*d*) $Bu = 0.25$); $Bu = 90$, Ro increasing from top to bottom ((*a*, *e*–*g*): (*a*) $Ro = 0.1$, (*e*) $Ro = 5$, (*f*) $Ro = 8$ and (*g*) $Ro = 10$). Thick grey lines correspond to unstable regions (non-zero Im(c)).
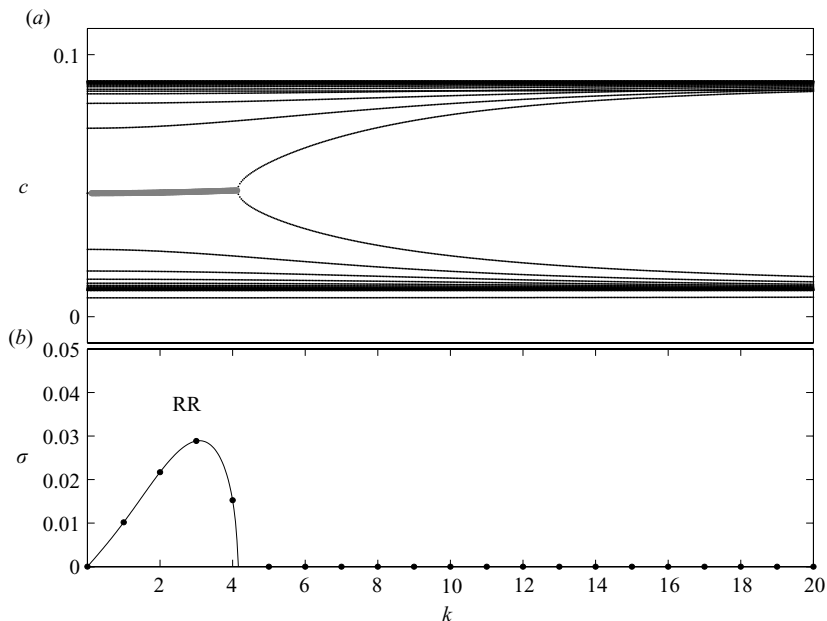
FIGURE 11. Dispersion diagram (*a*) and growth rate (*b*) of the modes for $Ro = 0.1$ and $Bu = 0.25$ (see (*a*) in figure 8). Grey line in (*a*) corresponds to the RR resonance and the respective unstable modes.

small R^* and KH instabilities at large F^*, which matches the traditional view of these instabilities. However, to keep a closer link with experimental results of Williams *et al.* (2005) the discussion below is based on Bu, Ro, F and d.

Thus, as for the ageostrophic Phillips model in a straight channel, cf. Gula *et al.* (2009), several types of instabilities are present, namely, (*a*) the baroclinic instability for small values of Bu and Ro (RR resonance), (*b*) the RK instability (RK or RP resonance) for intermediate values of Bu and Ro and (*c*) the KH instability (KK or KP resonance), for high values of Bu and Ro. As usual, the KH instability is characterized by highest growth rates and shortest wavelengths, the baroclinic instability is long wave and low growth rate and RK instability is intermediate, although spanning a wide range of wavenumbers. Note that the main difference with the plane-parallel flow of Gula *et al.* (2009) is the discrete selection of wavenumbers due to the annular geometry and the loss of the symmetry due to different heights and velocities at the inner and the outer wall.

In the figures 11–13 we give the dispersion diagrams (both real and imaginary parts of the phase speed as a function of the azimuthal wavenumber) corresponding to different values of (Ro, Bu) referring to typical cases (*a*), (*b*), (*c*), respectively, in figures 6–9. We present also the structure of unstable modes in both layers and the corresponding maps of the interface deviation, because this is often the measured quantity in experiments.

Figure 11 shows a dispersion diagram in the zone of baroclinic instability. Two Rossby waves, one propagating in each layer, are in resonance having the same Doppler shifted phase speed and give rise to a baroclinic instability (see Hoskins, McIntyre & Robertson 1985). The structure of the unstable mode is shown in figure 14.
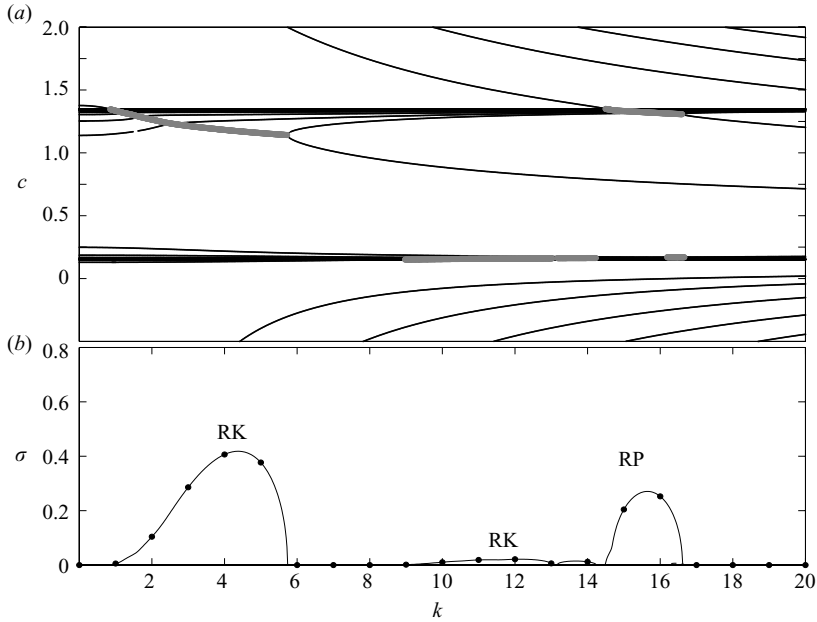
FIGURE 12. Dispersion diagram (*a*) and growth rate (*b*) of the modes for $Ro = 1.5$ and $Bu = 4$ (see (*b*) in figure 8). Thick grey lines in (*a*) correspond to the RK and RP resonances and the respective unstable modes.
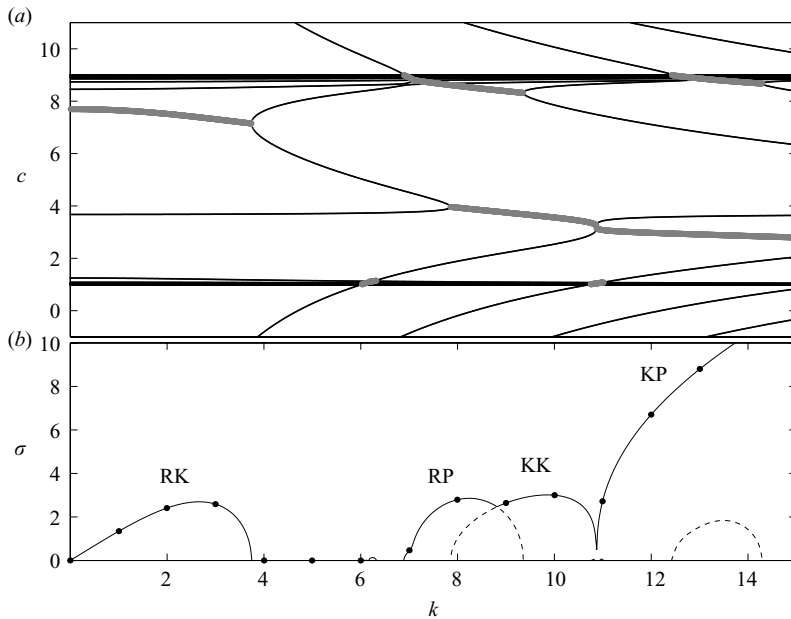

FIGURE 13. Dispersion diagram (*a*) and growth rate (*b*) of the modes for $Ro = 10$ and $Bu = 90$ (see (*c*) in figure 8). Thick grey lines in (*a*) correspond to the RK, KK, RP and KP resonances and the respective unstable modes.
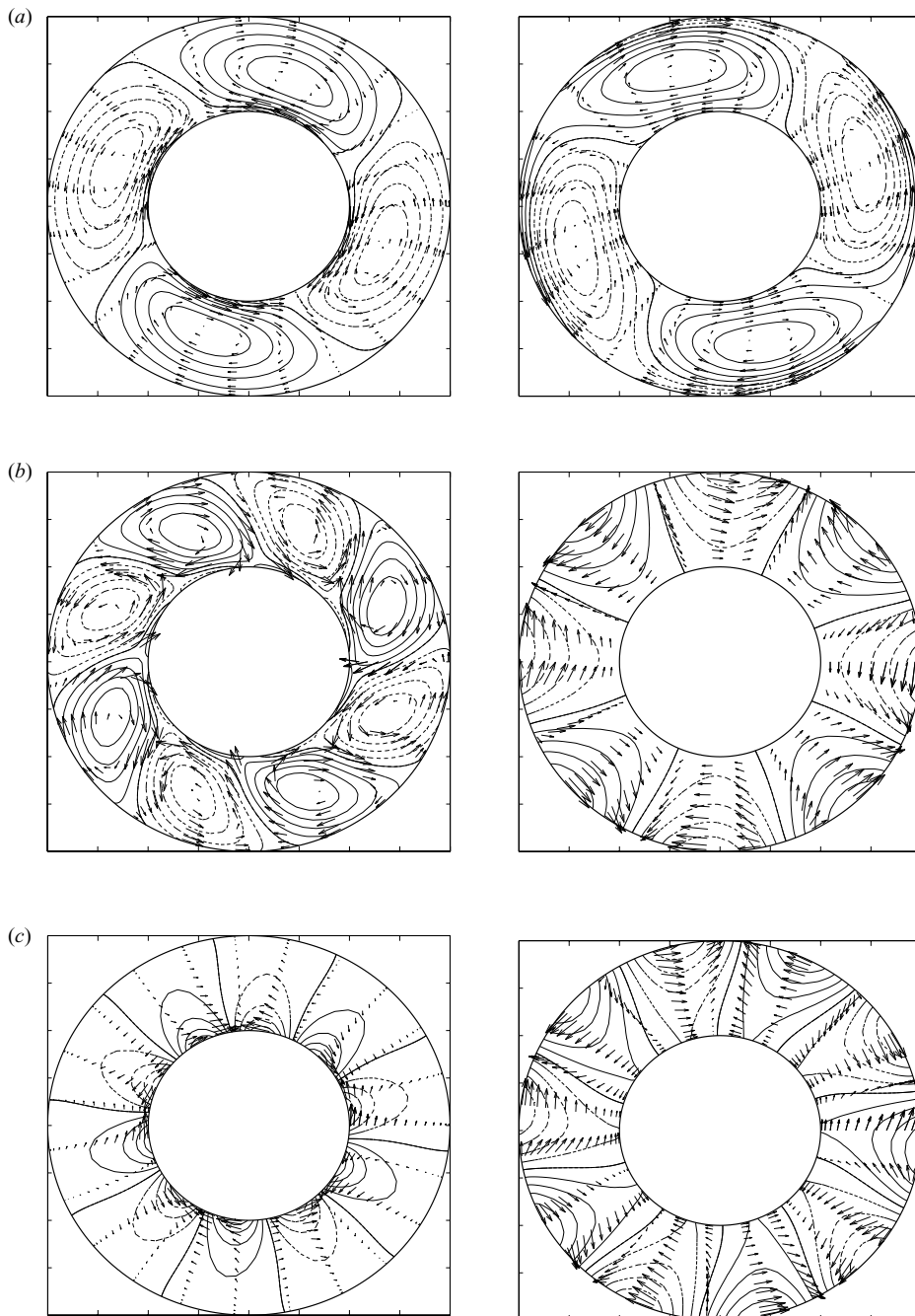
FIGURE 14. The structure, pressure and velocity fields of the upper (left) and lower layer (right), of (*a*) the baroclinically unstable mode at $k = 2$ (see figure 11), (*b*) the RK mode at $k = 4$ (see figure 12) and (*c*) the KH instability at $k = 5$ (see figure 13). The full lines correspond to positive and the dotted lines to negative values. (*a*) Both fields are typical of a Rossby mode. (*b*) The field in the upper layer is typical of a Rossby mode, while the field in the lower layer is typical of a Kelvin mode. (*c*) Both fields are typical of a Kelvin mode.
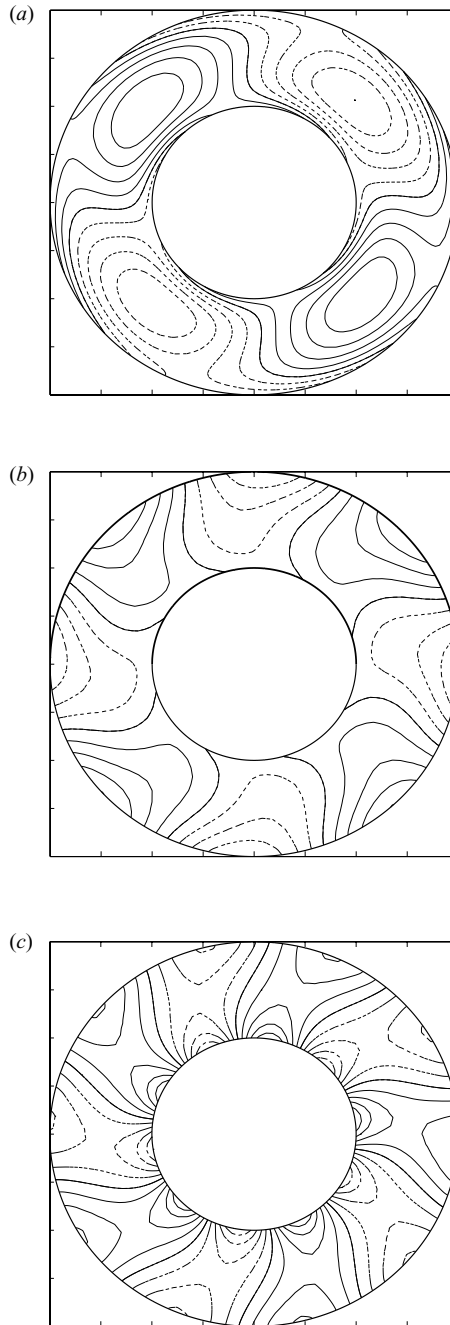
FIGURE 15. Interface height for (*a*) baroclinic instability at $k = 2$ (see figure 11), (*b*) RK instability at $k = 4$ (see figure 12) and (*c*) KH instability at $k = 5$ (see figure 13). The full lines correspond to positive and the dotted lines to negative values. Contours are plotted at the interval (*a*) 0.0137, (*b*) 0.015 and (*c*) 0.017.

Figure 12 shows a dispersion diagram in a pure RK instability area. A Rossby wave propagating in the upper layer resonates with a Kelvin wave propagating in the lower layer and give rise to a RK instability (see Sakai 1989; Gula *et al.* 2009). The structure of the unstable mode is shown in figure 14.
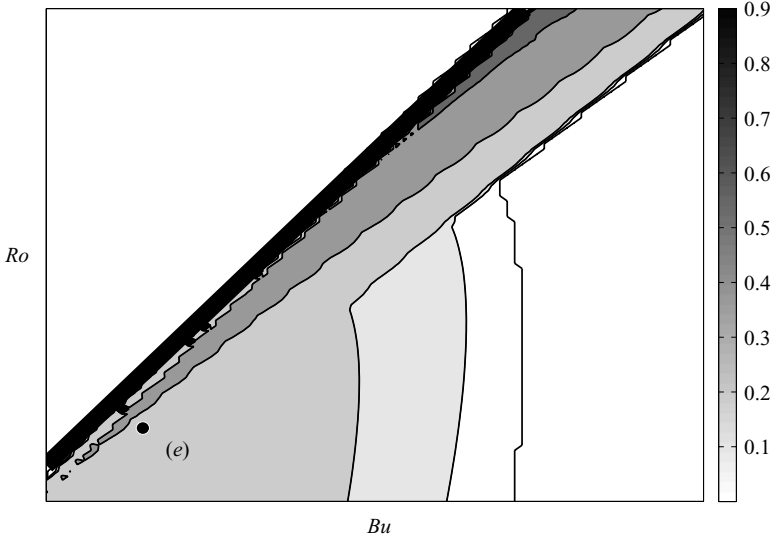
FIGURE 16. Growth rate of most unstable modes in (Ro, Bu) space. Zoom of the box in
figure 6. Contours displayed are 0.001, 0.01, 0.02 and further interval at 0.02.

Figure 13 shows a dispersion diagram in a KH instability area. A Kelvin wave propagating in the upper layer resonates with another Kelvin wave propagating in the lower layer and gives rise to a KH instability. For these values of parameters we can see that RP and RK instabilities are also present but with lower growth rates. The structure of the unstable mode is shown in figure 14.

Thus RK and KH instabilities coexist for large Bu and Ro (small F and d) having comparable growth rates, although different characteristic wavenumbers. As follows from the last figure, and from the comparison of figures 8 and 9, or 6 and 7, in general, close values of the growth rates may correspond to essentially different wavelengths of the most unstable modes. This means that different instabilities may coexist and compete. A clear-cut crossover region is indicated by a box in figures 8 and 9, and corresponds to coexisting baroclinic and RK instabilities. A zoom of the box is shown in figure 16.

Figure 17 shows the dispersion diagram corresponding to the (e) point in the crossover region of figure 16. We see that in this area both baroclinic and RK instability are present, having close growth rates. This means that the two instabilities are competing and that relatively high wavenumbers may be excited due to the RK instability in this range of parameters. The interface deviations corresponding to competing RR and RK instabilities are presented in figure 18.

4. Summary and discussion

Thus, after having analytically resolved the problem of small perturbations around cyclogeostrophycally balanced one-layer shallow-water Couette flow in the rotating annulus, which allowed us (a) to identify the normal modes of the problem and (b) to benchmark the numerical collocation scheme, we established a full stability diagram of the two-layer vertically sheared flow in the rotating annulus and identified the main instability modes. We established the origin of various instabilities resulting from phase-locking and resonance between the normal modes of the upper and the
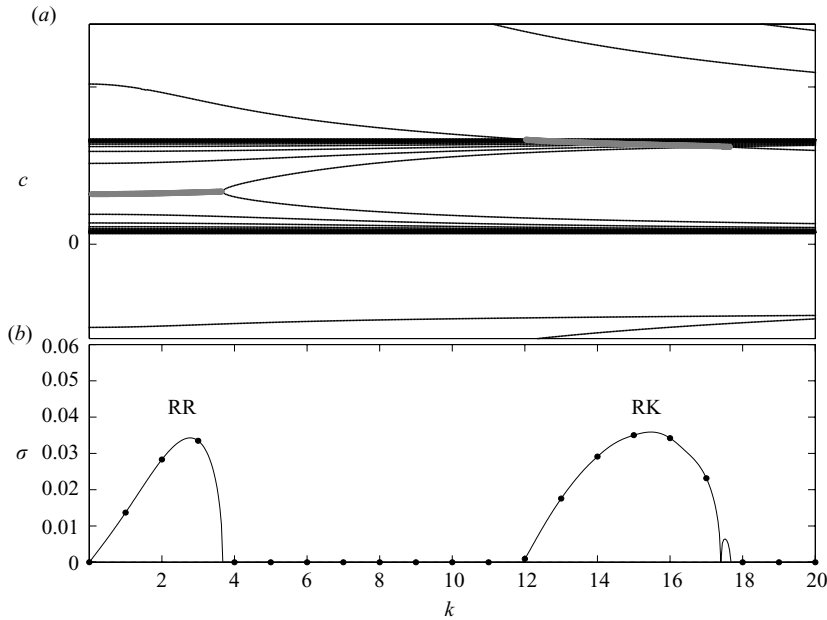
FIGURE 17. Dispersion diagram (*a*) and growth rate (*b*) of the modes for $Ro = 0.18$ and $Bu = 0.28$ (see (*e*) in figure 16). Thick grey lines in (*a*) correspond to the RR and RK resonances and the respective unstable modes.
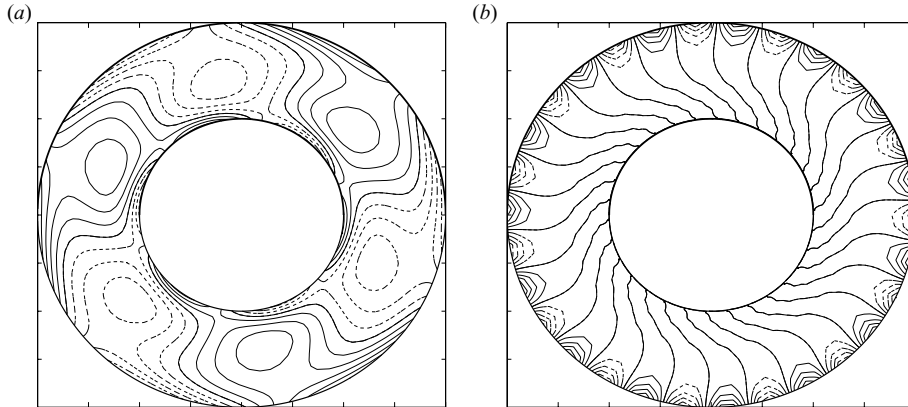

FIGURE 18. Interface height for baroclinic instability at $k = 4$ (*a*) and for RK instability at $k = 15$ (*b*). Both instabilities have the same growth rate for this set of (Ro, Bu) as can be seen on figure 17. The full lines correspond to positive and the dotted lines to negative values.

lower layer and showed different scenarios of stability loss in the space of parameters of the system. Perhaps the most interesting result is that in certain regions of the parameter space two different instabilities can exist and compete. The standard baroclinic instability, thus, may be 'contaminated' by the RK one. Remarkably, the corresponding crossover zone is situated in the domain of the parameter space where emergence of short-wave perturbations was observed in the experiments together with the developing baroclinic instability (cf. Williams *et al.* 2005). Although the RK instability has typical wavenumbers not sufficiently different from the baroclinic

one (cf. figure 17) and, thus, cannot directly explain the experimental observations of small-scale waves on top of the developing baroclinic instability, the interaction of two different unstable modes is worth studying in this context. Note that as shown in Gula *et al.* (2009), the nonlinear saturation of the RK instability is totally different from that of baroclinic instability, with an important role being played by the mean flow reorganisation. Thus, although on general grounds one could expect manifestations of the standard behaviour of the pair of nonlinear modes, like e.g. synchronization, it is difficult to make predictions without detailed studies of the nonlinear regime. The finite amplitude disturbances and the effects of nonlinearity as the nonlinear interactions between the various waves will be investigated in future work, both theoretically and by using a high-resolution finite-volume numerical scheme and a mesoscale atmospheric model (WRF).

Coming back to the main motivation of our study, the comparison between our results and laboratory experiments shows good agreement in some parameter regions, and discrepancies in some other. Let us look at the figure 8 and at the corresponding figure in Williams *et al.* (2005). While there is a very good agreement in the baroclinic instability region, the region of the KH instability in figure 8 is relatively narrow compared to Williams *et al.* (2005). As to the RK instability region, it is not clearly identifiable in the experiment.

An obvious explanation of the first discrepancy is that, in spite of the same physical mechanism, the KH instabilities in shallow-water and in full primitive equations are not quantitatively the same, especially in the large wavenumber domain. Another factor is surface tension. According to Hart (1972) and James (1977), the interfacial surface tension between the two layers is negligible for the long-wave instabilities, while it is stabilizing for short- wave ones. Indeed, the effect of interfacial surface tension is inversely proportional to the wavelength square. The short-wave RK and KH instabilities are then likely to be stabilized, while the long-wave baroclinic instability is unaffected.

Another possible explanation of non-manifestation of the RK instability is its rapid nonlinear saturation due to reorganisation of the mean flow and energy dissipation through small scale secondary KH instabilities (cf. Gula *et al.* 2009), which makes it more difficult to identify in a laboratory experiment such as Williams *et al.* (2005), especially in view of the small dimensions of the apparatus.

As was already stressed in the Introduction, the two-layer rotating shallow-water model should be considered as a conceptual one, allowing to grasp the universal features of destabilization of large-scale shear flows in GFD. In principle, a linear stability analysis of a full (three-dimensional, non-hydrostatic, viscous and surface tension included) experimental flow is possible along the same lines. However, such task requires incommensurate (with respect to its 'coarse-grained' shallow-water counterpart) computational efforts, and the results will depend on the fine structure of the mean flow (e.g. the parameters of the mixing layer between the layers) which may vary from one experiment to another.

REFERENCES

BALMFORTH, N. J. 1999 Shear instability in shallow water. *J. Fluid Mech.* **387**, 97–127.

CAIRNS, R. A. 1979 The role of negative energy waves in some instabilities of parallel flows. *J. Fluid Mech.* **92**, 1–14.

DUNKERTON, T., LELONG, P. & SNYDER, C. (ED.) 2008 Spontaneous imbalance. *J. Atmos. Sci.* webpage: `http://ams.allenpress.com/perlserv/?request=get-collection&coll_id=20&ct=1`.

FLOR, J. B. 2008 Frontal instability, inertia-gravity wave radiation and vortex formation. In *Proceedings of the ICMI International Conference on Multimodal Interfacings*, London, UK.

FORD, R. 1994 Gravity wave radiation from vortex trains in rotating shallow water. *J. Fluid Mech.* **281**, 81–118.

FULTZ, D., LONG, R. R., OWENS, G. V., BOHAN, W., KAYLOR, R. & WEIL, I. 1959 Studies of thermal convection in a rotating cylinder with some implications for large-scale atmospheric motions. *Meteorol. Monogr.* **4**, 1–104.

GRIFFITHS, R. W. & LINDEN, P. F. 1982 Part I. Density-driven boundary currents. *Geophys. Astrophys. Fluid Dyn.* **19**, 159–187.

GULA, J., PLOUGONVEN, R. & ZEITLIN, V. 2009 Ageostrophic instabilities of fronts in a channel in the stratified rotating fluid. *J. Fluid Mech.* **627**, 485–507.

HART, J. E. 1972 A laboratory study of baroclinic instability. *Geophys. Astrophys. Fluid Dyn.* **3**, 181–209.

HIDE, R. 1958 An experimental study of thermal convection in a rotating liquid. *Phil. Trans. R. Soc. Lond. Ser.* A*, Math. Phys. Sci.* **250** (983), 441–478.

HIDE, R. & FOWLIS, W. W. 1965 Thermal convection in a rotating annulus of liquid: effect of viscosity on the transition between axisymmetric and non-axisymmetric flow regimes. *J. Atmos. Sci.* **22**, 541–558.

HOSKINS, B. J., MCINTYRE, M. E. & ROBERTSON, A. W. 1985 On the use and significance of isentropic potential vorticity maps. *Quart. J. R. Meteorol. Soc.* **111** (470), 877–946.

JAMES, I. N. 1977 Stability of flow in a slowly rotating two-layer system. *Occasional Note Met Office 27/77/2* unpublished.

KILLWORTH, P. D. 1983 On the motion of isolated lenses on a beta-plane. *J. Phys. Oceanogr.* **13**, 368–376.

KNESSL, C. & KELLER, J. B. 1995 Stability of linear shear flows in shallow water. *J. Fluid Mech.* **303**, 203–214.

LOVEGROVE, A. F., READ, P. L. & RICHARDS, C. J. 2000 Generation of inertia-gravity waves in a baroclinically unstable fluid. *Quart. J. R. Meteorol. Soc.* **126**, 3233–3254.

O'SULLIVAN, D. & DUNKERTON, T. J. 1995 Generation of inertia-gravity waves in a simulated life cycle of baroclinic instability. *J. Atmos. Sci.* **52** (21), 3695–3716.

POULIN, F. J. & FLIERL, G. R. 2003 The nonlinear evolution of barotropically unstable jets. *J. Phys. Oceanogr.* **33**, 2173–2192.

SAKAI, S. 1989 Rossby–Kelvin instability: a new type of ageostrophic instability caused by a resonance between Rossby waves and gravity waves. *J. Fluid Mech.* **202**, 149–176.

STEWARTSON, K. 1957 On almost rigid rotations. *J. Fluid Mech.* **3**, 17–26.

TREFETHEN, L. N. 2000 *Spectral Methods in Matlab*. Society for Industrial and Applied Mathematics.

WILLIAMS, P. D., HAINE, T. W. N. & READ, P. L. 2005 On the generation mechanisms of short-scale unbalanced modes in rotating two-layer flows with vertical shear. *J. Fluid Mech.* **528**, 1–22.

WILLIAMS, P. D., READ, P. L. & HAINE, T. W. N. 2004 A calibrated, non-invasive method for measuring the internal interface height field at high resolution in the rotating, two-layer annulus. *Geophys. Astrophys. Fluid Dyn.* **98**, 453–471.